




Covariant density functional theory for nuclear fission based on a two-center harmonic oscillator basis

Zeyu Li ^{1,2}, Shengyuan Chen,² Minghui Zhou,² Yongjing Chen ^{1,*} and Zhipan Li ^{2,†}

¹*China Nuclear Data Center, China Institute of Atomic Energy, Beijing 102413, China*

²*School of Physical Science and Technology, Southwest University, Chongqing 400715, China*



(Received 7 September 2023; accepted 17 May 2024; published 10 June 2024)

Background: Nowadays, modern microscopic approaches for fission are generally based on the framework of nuclear density functional theory (DFT), which has enabled a self-consistent treatment of both static and dynamic aspects of fission. The key issue is a DFT solver with high precision and efficiency especially for the large elongated configurations.

Purpose: We aim to develop a DFT solver with high precision and efficiency based on the point coupling covariant density functional theory (CDFT), which has achieved great success in describing properties of nuclei for the whole nuclear chart.

Method: We have extended the point-coupling CDFT to be based on the two-center harmonic oscillator (TCHO) basis, which matches well with the large elongated configurations during the fission process. A multidimensional constraint and the time-dependent generator coordinate method (TDGCM) have been used to analyze the fission potential energy surface (PES) and fission dynamics, respectively. To simulate the splitting process of the nascent fragments beyond scission, we also introduce a density constraint into the new CDFT framework.

Results: Illustrative calculations have been done for the PESs and induced fission dynamics of two typical examples: ²²⁶Th and ²⁴⁰Pu. A more reasonable PES is obtained in the new framework compared to that based on the one-center harmonic oscillator (OCHO) with the same basis space. An optimization of about 0.2–0.3 MeV has been achieved for the outer fission barriers and large elongated configurations. The dynamical simulations based on CDFT-TCHO show an improved description of fission yields.

Conclusions: The newly developed CDFT solver optimizes the elongated configurations, improves the calculation efficiency, and provides a basis for large-scale multidimensional constraint calculations and dynamical simulations.

DOI: [10.1103/PhysRevC.109.064310](https://doi.org/10.1103/PhysRevC.109.064310)

I. INTRODUCTION

Nuclear fission presents a unique example of nonequilibrium large-amplitude collective motion where all nucleons participate with complex correlation effects, making the microscopic description of fission one of the most complex problems in low-energy theoretical nuclear physics [1,2]. Since the discovery of nuclear fission, various theories have been put forward and have enabled great progress. Based on the work of Bohr and Wheeler [3], the early theories for fission introduced a set of deformation parameters into the liquid drop model to construct multidimensional potential energy surfaces (PESs) to describe the relationship between nuclear deformation and energy, which gives a simple explanation of nuclear fission. In subsequent studies, the shell corrections and pair correlations were added to the liquid drop model, resulting in the macroscopic-microscopic (MM) approach [4,5]. The MM approach has a series of versions characterized by different parametrizations of the nuclear surface of the liquid drop and different phenomenological nuclear

potentials, such as the five-dimensional finite-range liquid-drop model (FRLDM) [6–8], the macroscopic-microscopic Woods-Saxon model [9,10], the macroscopic-microscopic Lublin-Strasbourg drop (LSD) model in the three-quadratic-surface parametrization [11,12], the LSD in Fourier shape parametrization [13], the two-center shell model [14], and so on. Based on a large number of parameters, the MM approach has greatly optimized the description of atomic nuclei. However, due to the parameter dependence of the results, the explanation of the microscopic mechanism of fission still eludes us.

Nowadays, modern microscopic approaches for fission are generally based on the framework of nuclear density functional theory (DFT), which has enabled a self-consistent treatment of both static and dynamic aspects of fission [1,15–19]. In the DFT framework that relies on the adiabatic approximation, the total energies and wave functions along the fission path are generally determined by the minimization of the energy density functional of the nucleus within a given set of constraints and assumed symmetries. Then the fission observables can be obtained by performing a time-dependent evolution of the collective wave packet on the microscopic PES using, e.g., the time-dependent generator coordinate method [20–35]. In this approach the dynamics of the

*ahchenyj@126.com

†zpliphy@swu.edu.cn

fissioning system essentially depends on the microscopic inputs, e.g., the PES and collective inertia as functions of few collective coordinates. However, the fully microscopic and nonadiabatic time-dependent DFT has shown that many collective degrees of freedom are excited in the fission process [36]. Therefore, to achieve a better description of fission dynamics based on DFT, one needs to carry out a larger-scale multidimensional calculation including more collective degrees of freedom. To this end, a DFT solver with high precision and efficiency especially for the large elongated configurations is necessary.

At present, based on the nonrelativistic density functionals, the popularly used DFT solvers for nuclear fission include, e.g., the codes HFBTHO [37] and HFODD [38,39] that solve the Skyrme Hartree-Fock-Bogolyubov (HFB) equations in the Cartesian deformed harmonic-oscillator (HO) basis, the code SKYAX [40] solving the Skyrme-Hartree-Fock equations on a two-dimensional mesh assuming axial symmetry, and the solvers for the HFB equation with the finite-range Gogny effective interaction in the deformed HO basis [41,42]. Based on the relativistic (covariant) framework, the multidimensional constrained CDFT in an axially deformed HO basis has been implemented [27,43], and, very recently, the time-dependent CDFT in three-dimensional lattice space has also been developed by means of the inverse Hamiltonian and spectral methods [44,45]. The constrained CDFT in deformed HO basis has been extensively used to study the spontaneous and induced fission dynamics, and achieved an acceptable agreement with the experimental data [27–31,46–48]. However, due to the mismatch between the one-center HO (OCHO) basis and the elongated configurations of the fissioning nucleus, both the accuracy and efficiency of the calculations decrease with the increase of elongation, and in particular, the calculation becomes unreliable for the configurations beyond scission. One way to solve this problem is to extend the present framework to be based on the two-center HO (TCHO) basis [49–51], which has been proved to be particularly well suited for the description of highly elongated systems [22,25,49].

In this work, we will extend the point-coupling CDFT to be based on the TCHO basis and perform illustrative calculations for the PESs and induced fission dynamics of two typical examples: ^{226}Th and ^{240}Pu . Moreover, we will implement the density constraint in the new developed CDFT and analyze the configurations and potential energy curve beyond scission. In Sec. II, the theoretical framework is introduced. The results for PESs and fragment yield distributions calculated based on CDFT in one-center and two-center HO bases are compared and discussed in detail in Sec. III. Density-constrained calculation for postscission configurations is briefly discussed in Sec. IV. Section V contains a summary of results and an outlook for future studies.

II. THEORETICAL FRAMEWORK

A. Covariant density functional theory

There is strong evidence that relativistic effects play an indispensable role in our understanding of the fine structure of

atoms/molecules and nuclei, although nonrelativistic methods were historically very popular and are still routinely utilized in modern studies. The most familiar manifestations of relativistic effects include the appearance of antifermions, their spin, and the resulting spin-orbit interactions, which form a key to understand the spin-orbit splitting of atomic spectra and nuclear single particle levels [52]. In recent decades, the relativistic (covariant) DFTs have been successfully applied to the study of nuclear static and dynamic properties [53–55]. Here, we will adopt CDFT to study nuclear fission, and the point-coupling version for CDFT can be written as

$$\begin{aligned}
 E_{\text{CDF}} &= \int d\mathbf{r} \varepsilon_{\text{CDF}}(\mathbf{r}) \\
 &= \sum_k \int d\mathbf{r} v_k^2 \bar{\psi}_k(\mathbf{r}) (-i\gamma \nabla + m) \psi_k(\mathbf{r}) \\
 &\quad + \int d\mathbf{r} \left(\frac{\alpha_S}{2} \rho_S^2 + \frac{\beta_S}{3} \rho_S^3 + \frac{\gamma_S}{4} \rho_S^4 + \frac{\delta_S}{2} \rho_S \Delta \rho_S \right. \\
 &\quad + \frac{\alpha_V}{2} j_\mu j^\mu + \frac{\gamma_V}{4} (j_\mu j^\mu)^2 + \frac{\delta_V}{2} j_\mu \Delta j^\mu + \frac{e}{2} \rho_p A^0 \\
 &\quad \left. + \frac{\alpha_{TV}}{2} j_{TV}^\mu (j_{TV})_\mu + \frac{\delta_{TV}}{2} j_{TV}^\mu \Delta (j_{TV})_\mu \right) \quad (1)
 \end{aligned}$$

with the local densities and currents

$$\begin{aligned}
 \rho_S(\mathbf{r}) &= \sum_k v_k^2 \bar{\psi}_k(\mathbf{r}) \psi_k(\mathbf{r}), \\
 j^\mu(\mathbf{r}) &= \sum_k v_k^2 \bar{\psi}_k(\mathbf{r}) \gamma^\mu \psi_k(\mathbf{r}), \\
 j_{TV}^\mu(\mathbf{r}) &= \sum_k v_k^2 \bar{\psi}_k(\mathbf{r}) \gamma^\mu \tau_3 \psi_k(\mathbf{r}), \quad (2)
 \end{aligned}$$

where ψ is the Dirac spinor field of the nucleon. ρ_p and A^0 are respectively the proton density and Coulomb field. The subscripts indicate the symmetry of the couplings: S stands for scalar, V for vector, and T for isovector. Various coupling constants (α , β , γ , δ) are determined by the PC-PK1 parametrization [56].

Minimizing the energy density functional Eq. (1) with respect to $\bar{\psi}_k$, one obtains the Dirac equation for the single nucleons,

$$\{-i\alpha \cdot \nabla + V(\mathbf{r}) + \beta[M + S(\mathbf{r})]\} \psi_k(\mathbf{r}) = \varepsilon_k \psi_k(\mathbf{r}), \quad (3)$$

where the local scalar $S(r)$ and vector $V(r)$ potentials are functions of densities and currents in the nucleus:

$$\begin{aligned}
 S(\mathbf{r}) &= \alpha_S \rho_S + \beta_S \rho_S^2 + \gamma_S \rho_S^3 + \delta_S \Delta \rho_S, \\
 V^\mu(\mathbf{r}) &= \alpha_V j^\mu + \gamma_V (j_\nu j^\nu) j^\mu + \delta_V \Delta j^\mu + e A^\mu \frac{1 - \tau_3}{2} \\
 &\quad + \tau_3 (\alpha_{TV} j_{TV}^\mu + \delta_{TV} \Delta j_{TV}^\mu). \quad (4)
 \end{aligned}$$

Solving Eqs. (2)–(4) iteratively, one can obtain the single-nucleon wave functions, densities, and currents, and also the binding energy of the nucleus E_{CDF} . Here, note that the Broyden method [57,58] was used in the iteration, which can speed up the convergences by about one order compared to the linear mixing for the elongated configurations.

Pairing correlations between nucleons are treated using the Bardeen-Cooper-Schrieffer (BCS) approach with a δ pairing force [59]. Due to the breaking of the translational symmetry, one has to consider the center-of-mass (c.m.) correction energy for the motion of the c.m., and here a phenomenological formula $E_{c.m.} = -\frac{3}{4} \times 41A^{-1/3}$ is adopted. Finally, the total energy is given by

$$E_{\text{tot}} = E_{\text{CDF}} + E_{\text{pair}} + E_{c.m.} \quad (5)$$

B. Two-center harmonic oscillator basis

To calculate the multidimensional PES in a large deformation space, one needs to solve the Dirac equation (3) with high precision and efficiency. When employing a one-center basis for calculation, theoretically, all possible configurations can be calculated as long as the basis space employed is sufficiently large. However, in practice, limited by the current level of computer technology, it is impossible to construct a basis space large enough, which hinders us from performing large-scale multidimensional calculations. Solving the Dirac equation based on a two-center basis may be an effective method to improve the precision and efficiency [60]. Therefore, in this work, we expand the Dirac spinor in a two-center harmonic oscillator (TCHO) basis to match the large elongated configuration during fission. The axially symmetric TCHO potential in cylindrical coordinate system reads

$$V(r_{\perp}, z) = \frac{1}{2}M\omega_{\perp}^2 r_{\perp}^2 + \begin{cases} \frac{1}{2}M\omega_1^2(z+z_1)^2, & z < 0, \\ \frac{1}{2}M\omega_2^2(z-z_2)^2, & z \geq 0, \end{cases} \quad (6)$$

where M is the nucleon mass. TCHO can be regarded as two off-center harmonic oscillators connected at $z = 0$, while z_1 (z_2) and ω_1 (ω_2) denote the distance from $z = 0$ to the center of the left (right) harmonic oscillator and its frequency, respectively.

Due to the spatial rotational symmetry along z axis, the eigenfunction of TCHO can be written as the product of eigenfunctions of different degrees of freedom,

$$\Phi(r_{\perp}, z, \theta, s) = \phi_{n_r}^{m_l}(r_{\perp})\phi_{\nu}(z)\frac{1}{\sqrt{2\pi}}e^{im_l\theta}\chi_{m_s} \quad (7)$$

with

$$\phi_{n_r}^{m_l}(r_{\perp}) = \frac{\sqrt{2}}{b_{\perp}}\sqrt{\frac{n_r!}{(n_r+m_l)!}}\eta^{m_l/2}L_{n_r}^{m_l}(\eta)e^{-\eta/2}, \quad (8)$$

$$\phi_{\nu}(z) = \begin{cases} C_{\nu_1}H_{\nu_1}(-\zeta_1)e^{-\zeta_1^2/2} & \text{for } z < 0, \\ C_{\nu_2}H_{\nu_2}(\zeta_2)e^{-\zeta_2^2/2} & \text{for } z \geq 0, \end{cases} \quad (9)$$

where $\eta = r_{\perp}^2/b_{\perp}^2$, $\zeta_1 = (z+z_1)/b_1$, and $\zeta_2 = (z-z_2)/b_2$. b_{\perp} , b_1 , and b_2 are the characteristic lengths obeying the general relationship $b = \sqrt{\hbar/M\omega}$ with their corresponding frequencies. $L_{n_r}^{m_l}(\eta)$ and $H_{\nu}(\zeta)$ denote the associated Laguerre polynomial and Hermite function, respectively. In Eq. (9), ν_1 , ν_2 , C_{ν_1} , and C_{ν_2} are determined by four conditions: continuity of $\phi_{\nu}(z)$ and $\phi'_{\nu}(z)$ at $z = 0$, stationary condition of eigenenergy, and normalization [51]. For the convenience of discussion and application, we set $z_1 = z_2$, $b_1 = b_2$ and denote the TCHO basis as $|\alpha\rangle = |n_r, \nu, m_l, m_s\rangle$ in the following.

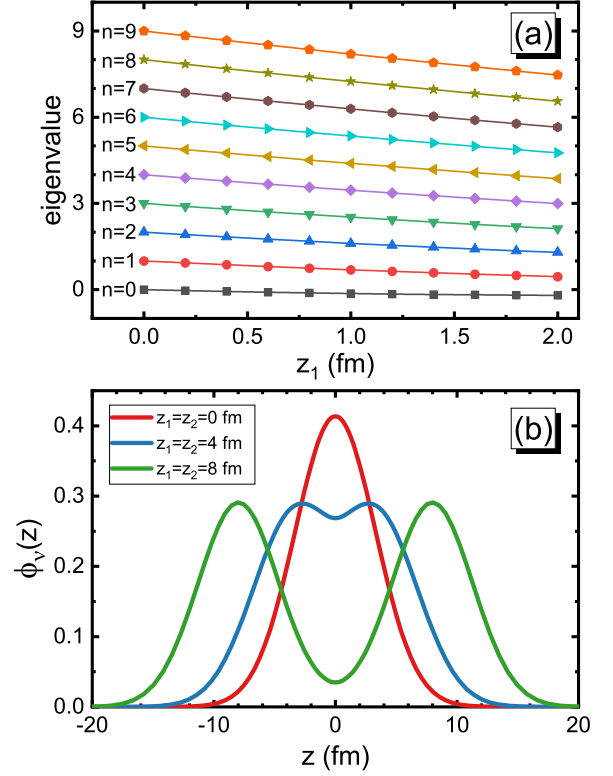


FIG. 1. Evolution of the eigenvalue ν_1 (a) and the wave function $\phi_{\nu}(z)$ of the ground state (b) with increasing z_1 for fixed $b_1 = 3.3$ fm.

The choice of parameters z_1 and b_1 is introduced in detail in Appendix A.

To get an intuitional impression of the TCHO basis, in Fig. 1, we show the evolution of the eigenvalue ν_1 and the wave function $\phi_{\nu}(z)$ of the ground state with increasing z_1 . Obviously, the eigen quantum numbers are not integers when $z_1 \neq 0$, and the levels become denser for larger z_1 . Remarkably, the evolution of the wave function is consistent with that of the configurations in the fission process by adopting deformation-dependent basis parameters, which is introduced in detail in Appendix A. For configurations with small deformations, TCHO reduces to OCHO (specifically, $z_1 = z_2 = 0$ when $\beta_2 < 1$). As the nucleus elongates and the two fragments are forming, the basis employed gradually changes from one center to two center, ensuring consistency with the evolving density distribution.

To solve the Dirac equation (3) in the TCHO basis, first we expand the Dirac spinor ψ_k as

$$\psi_k(r, s) = \begin{pmatrix} f_k(r, s) \\ ig_k(r, s) \end{pmatrix} = \begin{pmatrix} \sum_{\alpha} f_{\alpha}^k |\alpha\rangle \\ i \sum_{\bar{\alpha}} g_{\bar{\alpha}}^k |\bar{\alpha}\rangle \end{pmatrix}. \quad (10)$$

The summation of α has to be truncated for a given number of shells N_f which satisfies $E_{\alpha} \leq (N_f + 3/2)\hbar\omega$ with $\hbar\omega = 41A^{-1/3}$ MeV, and the summation of $\bar{\alpha}$ is truncated at $N_g = N_f + 1$ to avoid spurious states. Then we obtain the

Dirac equation in matrix form,

$$\begin{pmatrix} A_{\alpha,\alpha'} & B_{\alpha,\bar{\alpha}'} \\ B_{\bar{\alpha},\alpha'} & -C_{\bar{\alpha},\bar{\alpha}'} \end{pmatrix} \begin{pmatrix} f_{\alpha'}^k \\ g_{\bar{\alpha}'}^k \end{pmatrix} = \varepsilon_k \begin{pmatrix} f_{\alpha}^k \\ g_{\bar{\alpha}}^k \end{pmatrix}. \quad (11)$$

The matrix elements $A_{\alpha,\alpha'}$, $B_{\alpha,\bar{\alpha}'}$, and $C_{\bar{\alpha},\bar{\alpha}'}$ can be expressed as follows:

$$\begin{aligned} A_{\alpha,\alpha'} &= \delta_{m_i m_i'} \delta_{m_s m_s'} N_{n_r}^{m_i} N_{n_r'}^{m_i'} \int_0^\infty d\eta e^{-\eta} \eta^{m_i} L_{n_r}^{m_i}(\eta) L_{n_r'}^{m_i'}(\eta) \\ &\times \left[C_{v_1} C_{v_1'} \int_{-\infty}^0 dz e^{-\xi_1^2} H_{v_1}(-\xi_1) H_{v_1'}(-\xi_1) \right. \\ &\left. + C_{v_2} C_{v_2'} \int_0^\infty dz e^{-\xi_2^2} H_{v_2}(\xi_2) H_{v_2'}(\xi_2) \right] \\ &\times [M + S(r_\perp, z) + V(r_\perp, z)], \end{aligned} \quad (12)$$

$$\begin{aligned} C_{\bar{\alpha},\bar{\alpha}'} &= \delta_{m_i m_i'} \delta_{m_s m_s'} N_{n_r}^{m_i} N_{n_r'}^{m_i'} \int_0^\infty d\eta e^{-\eta} \eta^{m_i} L_{n_r}^{m_i}(\eta) L_{n_r'}^{m_i'}(\eta) \\ &\times \left[C_{v_1} C_{v_1'} \int_{-\infty}^0 dz e^{-\xi_1^2} H_{v_1}(-\xi_1) H_{v_1'}(-\xi_1) \right. \\ &\left. + C_{v_2} C_{v_2'} \int_0^\infty dz e^{-\xi_2^2} H_{v_2}(\xi_2) H_{v_2'}(\xi_2) \right] \\ &\times [M + S(r_\perp, z) - V(r_\perp, z)], \end{aligned} \quad (13)$$

$$\begin{aligned} B_{\alpha,\bar{\alpha}'} &= \delta_{m_i m_i'} \delta_{m_s m_s'} \delta_{n_r n_r'} (-1)^{\frac{1}{2} - m_s} I_1(v, v') \\ &+ \delta_{v v'} \delta_{m_i m_i' - 1} \delta_{m_s m_s' + 1} \frac{N_{n_r}^{m_i} N_{n_r'}^{m_i'}}{b_\perp} \int_0^\infty d\eta e^{-\eta} \\ &\times \eta^{m_i/2} \eta^{(m_i' - 1)/2} L_{n_r}^{m_i}(\eta) \left(\tilde{L}_{n_r'}^{m_i'}(\eta) + m_i' L_{n_r'}^{m_i'}(\eta) \right) \\ &+ \delta_{v v'} \delta_{m_i m_i' + 1} \delta_{m_s m_s' - 1} \frac{N_{n_r}^{m_i} N_{n_r'}^{m_i'}}{b_\perp} \int_0^\infty d\eta e^{-\eta} \\ &\times \eta^{m_i/2} \eta^{(m_i' - 1)/2} L_{n_r}^{m_i}(\eta) \left(\tilde{L}_{n_r'}^{m_i'}(\eta) - m_i' L_{n_r'}^{m_i'}(\eta) \right), \end{aligned} \quad (14)$$

with

$$\begin{aligned} I_1(v, v') &= \frac{C_{v_1} C_{v_1'}}{b_1} \int_{-\infty}^0 dz e^{-\xi_1^2} H_{v_1}(-\xi_1) \\ &\times [\xi_1 H_{v_1}(-\xi_1) + H_{v_1+1}(-\xi_1)] \\ &+ \frac{C_{v_2} C_{v_2'}}{b_2} \int_0^\infty dz e^{-\xi_2^2} H_{v_2}(\xi_2) \\ &\times [\xi_2 H_{v_2}(\xi_2) - H_{v_2+1}(\xi_2)]. \end{aligned} \quad (15)$$

Finally, we can obtain the single nucleon energies and wave functions by diagonalizing the Hamiltonian matrix. In the following, we will denote the new implementation of CDFT based on TCHO basis as CDFT-TCHO.

C. Multidimensional constraint calculation

The entire map of the energy surface in multidimensional collective space for fission is obtained by imposing constraints on a number of collective coordinates, e.g., axial quadrupole

and octupole moments q_2, q_3 , and the number of nucleons in the neck q_N ,

$$\langle E_{\text{tot}} \rangle + \sum_{k=2,3} C_k (\langle \hat{Q}_k \rangle - q_k)^2 + C_N (\langle \hat{Q}_N \rangle - q_N)^2, \quad (16)$$

where $\langle E_{\text{tot}} \rangle$ is the total energy of CDFT, C_k and C_N are the corresponding stiffness constants. \hat{Q}_2, \hat{Q}_3 , and \hat{Q}_N denote the mass quadrupole and octupole operators, and the Gaussian neck operator, respectively:

$$\begin{aligned} \hat{Q}_2 &= 2z^2 - r_\perp^2. \\ \hat{Q}_3 &= 2z^3 - 3zr_\perp^2. \\ \hat{Q}_N &= e^{-(z-z_N)^2/a_N^2}, \end{aligned} \quad (17)$$

where $a_N = 1$ fm and z_N is the position of the neck determined by minimizing $\langle \hat{Q}_N \rangle$ [42]. The left and right fragments are defined as parts of the whole nucleus with $z \leq z_N$ and $z \geq z_N$, respectively.

The widely used quadrupole and octupole deformation parameters β_2 and β_3 can be determined from the following relations:

$$\beta_2 = \frac{\sqrt{5\pi}}{3AR_0^2} \langle \hat{Q}_2 \rangle, \quad (18)$$

$$\beta_3 = \frac{\sqrt{7\pi}}{3AR_0^3} \langle \hat{Q}_3 \rangle, \quad (19)$$

with $R_0 = r_0 A^{1/3}$ and $r_0 = 1.2$ fm.

When the configurations for the full collective space are obtained under the constrained calculations, we can finally determine the collective PES by subtracting the energy of zero-point motion, e.g., the vibrational and rotational zero-point motions:

$$V(\beta_2, \beta_3, q_N, \dots) = E_{\text{tot}} - \Delta E_{\text{vib}} - \Delta E_{\text{rot}}. \quad (20)$$

The zero-point energy (ZPE) corrections are calculated in the cranking approximation [61], and the expression for vibrational ZPE reads

$$\Delta E_{\text{vib}} = \frac{1}{4} \text{Tr}[\mathcal{M}_{(3)}^{-1} \mathcal{M}_{(2)}], \quad (21)$$

with

$$\mathcal{M}_{(n),kl} = \sum_{i,j} \frac{\langle i | \hat{Q}_k | j \rangle \langle j | \hat{Q}_l | i \rangle}{(E_i + E_j)^n} (u_i v_j + v_i u_j)^2, \quad (22)$$

where E_i and v_i are the quasiparticle energies and occupation probabilities, respectively. The summation is over the proton and neutron single-particle states in the canonical basis. The rotational ZPE takes the form

$$\Delta E_{\text{rot}} = \frac{\langle \hat{J}^2 \rangle}{2\mathcal{I}}, \quad (23)$$

where \mathcal{I} is the Inglis-Belyaev moment of inertia [62,63].

For the dynamical simulation, one also needs to calculate the mass tensor in the perturbative cranking approximation [61]:

$$B_{kl}(\beta_2, \beta_3, q_N, \dots) = \hbar^2 [\mathcal{M}_{(1)}^{-1} \mathcal{M}_{(3)} \mathcal{M}_{(1)}^{-1}]_{kl}. \quad (24)$$

D. Time-dependent generator coordinate method

Based on the adiabatic approximation for low-energy fission, the nucleon degree of freedom is decoupled from the collective degrees of freedom. Therefore, the nuclear wave function $|\Phi\rangle$ is represented as a superposition of intrinsic states $|\varphi(\beta)\rangle$ calculated by the CDFT:

$$|\Phi(t)\rangle = \int f(\beta, t) |\varphi(\beta)\rangle d\beta, \quad (25)$$

where f represents the corresponding weight function. It is noted that the intrinsic state $\varphi(\beta)$ is chosen as a Slater determinant composed of a series of Dirac spinors in Eq. (3). Correspondingly, the nuclear wave function satisfies the time-dependent equation

$$i\hbar\partial_t|\Phi\rangle = \hat{H}|\Phi\rangle. \quad (26)$$

where \hat{H} is the Hamiltonian of the nuclear system determined by CDFT. In the current relativistic framework, the equation is naturally expressed as first-order derivatives with respect to both time and space for the nuclear system composed of Dirac particles.

Applying the variational principle yields the equation of motion for the weight function, known as the Griffin-Hill-Wheeler equation,

$$i\hbar\mathcal{N}\partial_t f = \mathcal{H}f \quad (27)$$

with the normal overlap kernel \mathcal{N} and Hamiltonian kernel \mathcal{H}

$$\begin{aligned} \mathcal{N}(\beta', \beta) &= \langle\varphi(\beta')|\varphi(\beta)\rangle, \\ \mathcal{H}(\beta', \beta) &= \langle\varphi(\beta')|\hat{H}|\varphi(\beta)\rangle. \end{aligned} \quad (28)$$

The weight function f is not a probability amplitude of finding the system at the collective coordinate β due to the non-orthogonality of the basis. Thus, a transformation should be done first [64]:

$$\begin{aligned} g &= \mathcal{N}^{\frac{1}{2}} f, \\ H_{\text{coll}} &= \mathcal{N}^{-\frac{1}{2}} \mathcal{H} \mathcal{N}^{-\frac{1}{2}}. \end{aligned} \quad (29)$$

Then we employ the Gaussian overlap approximation (GOA) for the normal kernel \mathcal{N} and expand the collective Hamiltonian up to second-order derivatives of collective coordinates [64]. Finally, a local collective Hamiltonian is obtained, and the equation of motion for the collective wave function in the (β_2, β_3) space is as follows:

$$\begin{aligned} i\hbar\frac{\partial}{\partial t}g(\beta_2, \beta_3, t) &= \left[-\frac{\hbar^2}{2} \sum_{kl} \frac{\partial}{\partial\beta_k} B_{kl}^{-1}(\beta_2, \beta_3) \frac{\partial}{\partial\beta_l} + V(\beta_2, \beta_3) \right] \\ &\times g(\beta_2, \beta_3, t), \end{aligned} \quad (30)$$

where $g(\beta_2, \beta_3, t)$ is a complex wave function, which contains all the information about the dynamics of the system. $V(\beta_2, \beta_3)$ and $B_{kl}(\beta_2, \beta_3)$ are the collective potential and mass tensor, respectively, which are derived from the CDFT Hamiltonian kernel in Eq. (28) and completely determine

the dynamics of the fission process in the TDGCM+GOA framework. The probability current is defined by

$$\begin{aligned} J_k(\beta_2, \beta_3, t) &= \frac{\hbar}{2i} \sum_{l=2}^3 B_{kl}^{-1}(\beta_2, \beta_3) \left[g^*(\beta_2, \beta_3, t) \frac{\partial g(\beta_2, \beta_3, t)}{\partial\beta_l} \right. \\ &\quad \left. - g(\beta_2, \beta_3, t) \frac{\partial g^*(\beta_2, \beta_3, t)}{\partial\beta_l} \right]. \end{aligned} \quad (31)$$

Starting from an initial state of the compound nucleus, the collective current will move to a large deformation region and pass through a so-called scission line that is composed of the hypersurface at which the nucleus splits. At the time t , the measurement of the probability of a given pair of fragments can be calculated by integrating the probability current which runs through the scission line. For a surface element ξ , the sum of the time-integrated flux of the probability $F(\xi, t)$ can be written as [65]

$$F(\xi, t) = \int_{t=0}^t dt \int_{(\beta_2, \beta_3) \in \xi} \mathbf{J}(\beta_2, \beta_3, t) \cdot d\mathbf{S}. \quad (32)$$

For each point on the scission line, it contains the information of (A_L, A_H) , which represent the masses of light and heavy fragments, respectively. Hence the yield of fission fragments with mass A can be defined formally as

$$Y(A) \propto \sum_{\xi \in \mathcal{A}} \lim_{t \rightarrow +\infty} F(\xi, t), \quad (33)$$

where \mathcal{A} is the set of all elements ξ belonging to the scission line such that the heavy or light fragment has mass A . Here, we will use the software package FELIX-2.0 [65] to solve the time-dependent Schrödinger-like equation and calculate the fission observables.

III. ILLUSTRATIVE CALCULATIONS FOR ^{226}Th AND ^{240}Pu

In this section, we present the illustrative calculations for two typical examples: ^{226}Th and ^{240}Pu . Specifically, we will compare the PESs, scission lines, and fragment yield distributions calculated based on CDFT in OCHO and TCHO bases to demonstrate the improvement of the computing efficiency and accuracy of CDFT-TCHO. In the CDFT framework, the energy density functional PC-PK1 [56] determines the effective interaction in the particle-hole channel, and a δ force is used in the particle-particle channel. The strength parameters of the δ force are $V_n (V_p) = 360 (378) \text{ MeV fm}^3$ and $V_n (V_p) = 338 (372.5) \text{ MeV fm}^3$ for ^{226}Th and ^{240}Pu , respectively, which are determined by reproducing the empirical pairing gaps from a five-point formula [66].

In the first step, a large-scale deformation-constrained CDFT calculation is performed to generate the PESs, scission lines, and mass tensors in the β_2 - β_3 plane. The range of collective variables is -0.98 to 6.98 for β_2 with a step $\Delta\beta_2 = 0.04$, and from 0.00 to 4.24 for β_3 with a step $\Delta\beta_3 = 0.08$. When describing fission in a collective space, scission is characterized by a discontinuity between the two domains of prescissioned and postscissioned configurations. Following our previous study [27], here we define the prescission domain

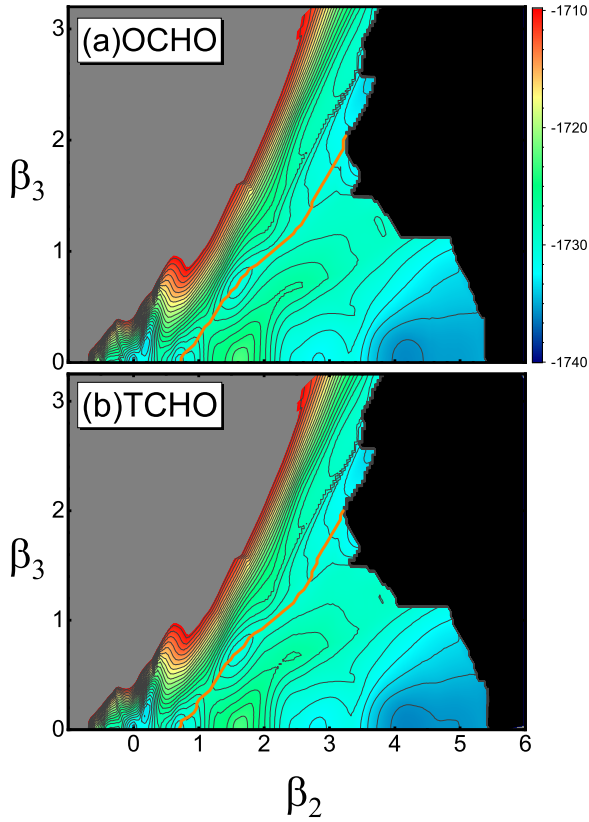


FIG. 2. The potential energy surfaces of ^{226}Th in the β_2 - β_3 plane calculated using the CDFT in OCHO (a) and TCHO (b) bases with a cutoff of major shell $N_f = 20$. The orange solid line denotes the optimal fission path.

by the nucleon number in the neck $q_N \geq 3$ and consider the frontier of this domain as the scission line.

For the induced fission dynamics, the TDGCM+GOA is performed to model the time evolution of the fissioning nucleus with a time step $\delta t = 5 \times 10^{-4}$ zs. The parameters of the additional imaginary absorption potential that takes into account the escape of the collective wave packet in the domain outside the region of calculation are the absorption rate $r = 20 \times 10^{22} \text{ s}^{-1}$ and the width of the absorption band, $w = 1.5$.

A. Results for ^{226}Th

Figure 2 displays the PESs of ^{226}Th in the β_2 - β_3 plane calculated using the CDFT in OCHO and TCHO bases with a cutoff of major shell $N_f = 20$. The orange solid line denotes the optimal fission path. The topographies of these two PESs look almost same on the whole, and are also comparable with that obtained using the Hartree-Fock-Bogoliubov framework based on the Gogny D1S functional [67]. Two competing fission valleys, i.e., the asymmetric one passing by the optimal fission path and the symmetric one with $\beta_3 \approx 0$, are observed and they are separated by a ridge from $(\beta_2, \beta_3) \approx (1.5, 0.0)$ to $(3.8, 1.2)$.

To compare the two calculations in more detail, we present the potential energy curves along both the asymmetric and symmetric fission paths in Fig. 3. The potential energies for

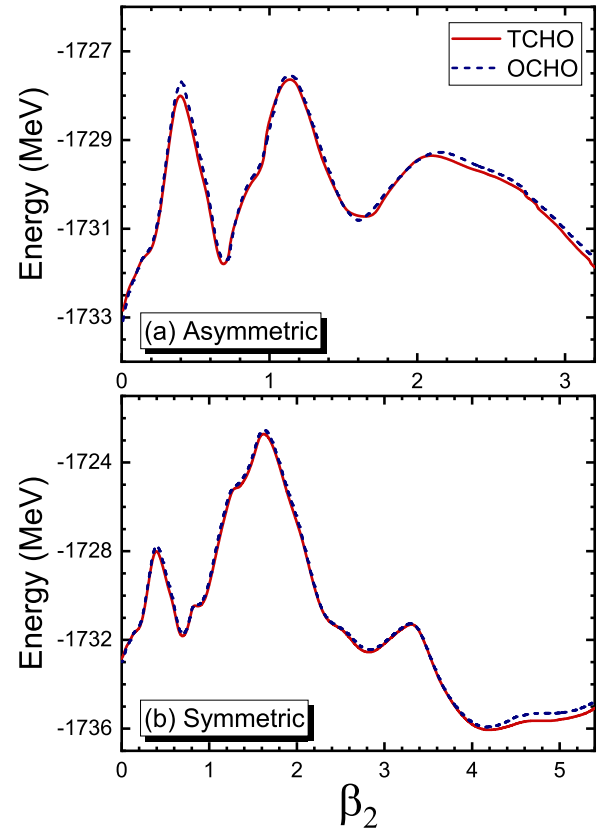


FIG. 3. The potential energy curves along the asymmetric (a) and symmetric (b) fission paths of ^{226}Th calculated using CDFT in TCHO and OCHO bases.

the fission barriers and large elongated configurations calculated using TCHO are generally lower than those of OCHO. Specifically, along the asymmetric path, a triple-humped fission barrier is predicted, and the calculated heights using TCHO (OCHO) are 5.92 (6.11), 6.05 (6.25), and 4.32 (4.51) MeV from the inner to the outer barrier, respectively. The barrier heights along the symmetric path are 5.92 (6.11), 10.99 (11.30), and 2.37 (2.52) MeV from inner to outer. Please note that here the values for the calculation with OCHO basis are different from those in our previous work [27] due to the consideration of the vibrational and rotational ZPEs [cf. Eq. (20)] in current work. Moreover, we also find that the ridge between two fission paths is lowered, e.g., ≈ 0.1 MeV for $(\beta_2, \beta_3) = (3.46, 1.20)$.

To check the efficiency of CDFT-TCHO, we take the more elongated symmetric fission path as an example to compare the computing time for three cases: TCHO with a cutoff of major shell $N_f = 20$, and OCHO with $N_f = 20$ and $N_f = 24$, in Fig. 4. For the first two calculations, the computing time is similar, $\lesssim 300$ s for most of the configurations, but the accuracy of TCHO is better, ≈ 0.3 MeV lower for the large deformations due to the match between bases and calculated configurations. To get accuracy similar to that of TCHO, the OCHO basis space has to be enlarged to $N_f = 24$, which of course consumes more time, about twice that of TCHO calculation. Moreover, the extremely large computing time

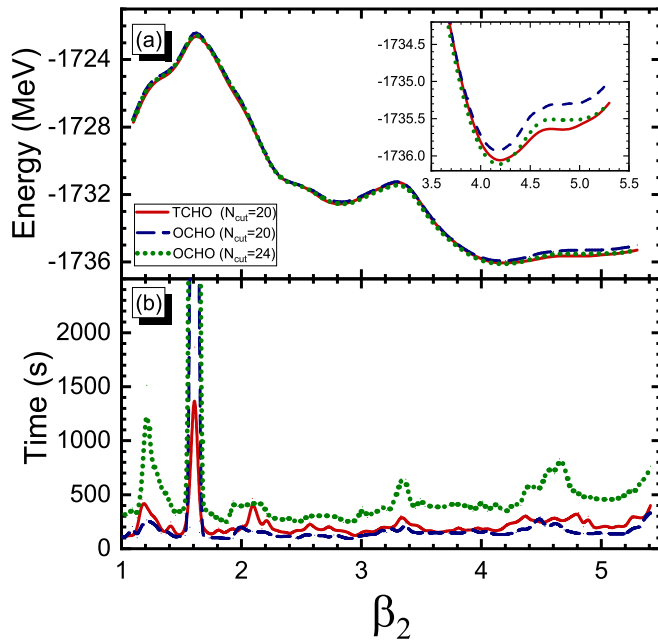


FIG. 4. The potential energy curves (a) and computing time (b) for the symmetric fission path of ^{226}Th calculated using CDFT in TCHO and OCHO bases. The solid, dashed, and dotted curves correspond to the results calculated from TCHO with a cutoff of major shell $N_f = 20$ and from OCHO with $N_f = 20$ and $N_f = 24$, respectively. The inset of panel (a) displays the potential energy curves for large deformations.

for the configurations around the second fission barrier $\beta_2 \approx 1.6$, $\approx 33\,000$ s by CDFT-OCHO, is significantly reduced to ≈ 1800 s by CDFT-TCHO. This is very important for the large-scale multidimensional calculations that are crucial for high-precision description of fission dynamics.

Figure 5 displays the scission lines of ^{226}Th in the β_2 - β_3 plane calculated using CDFT in TCHO and OCHO bases. Their patterns are very similar and there is only a little difference at the ends of the symmetric and asymmetric

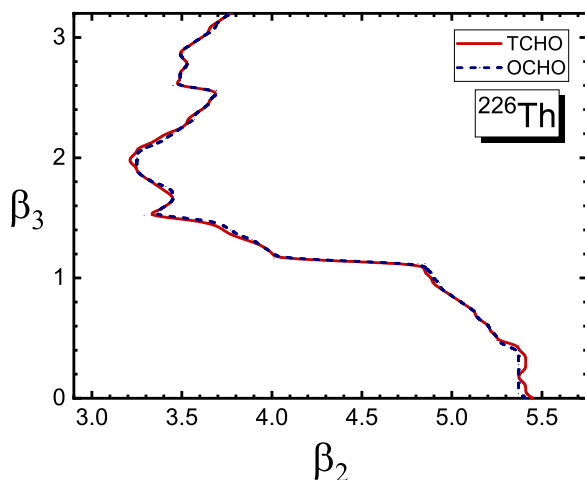


FIG. 5. The scission lines of ^{226}Th in the β_2 - β_3 plane calculated using CDFT in TCHO and OCHO bases.

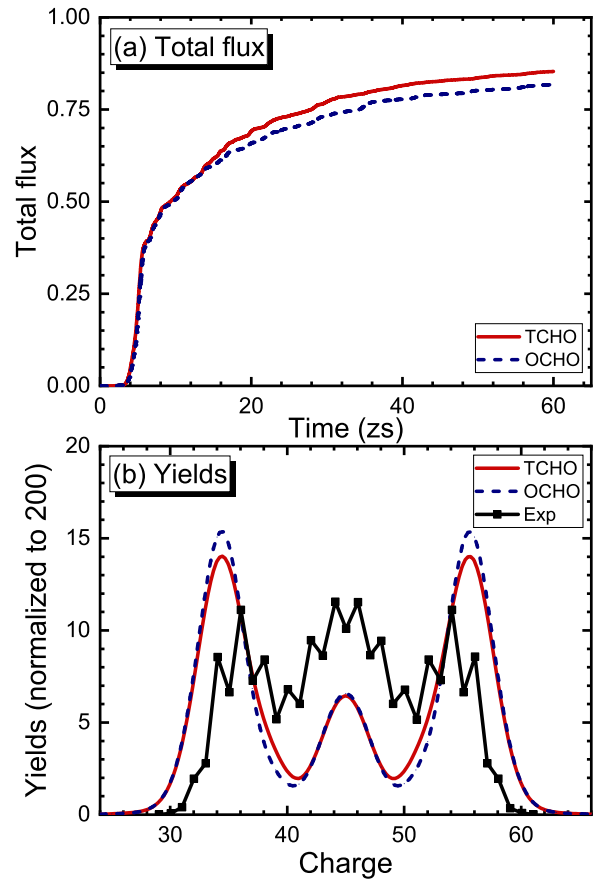


FIG. 6. Total flux as a function of time (a) and preneutron emission charge yields (b) for the photoinduced fission of ^{226}Th calculated by TDGCM+GOA based on CDFT in OCHO and TCHO bases. The experimental charge yields are also shown for comparison [68].

fission valleys, i.e. $\beta_3 \approx 0.0$ and 2.0. In addition, we have also checked the mass tensors B_{22} and B_{33} calculated using Eq. (24) and the relative root-mean-square discrepancy is within 0.03%.

Using the PESs, mass tensor, and scission configurations as inputs, we can simulate the dynamics for the photoinduced fission of ^{226}Th in the framework of TDGCM+GOA. Following the procedure of Ref. [27], The initial state is prepared by boosting the collective ground state in the direction of β_2 with a target excitation energy about 11 MeV [68]. Figure 6 displays the time evolution of total flux that passes through the scission line [panel (a)] and the preneutron emission charge yields [panel (b)] for ^{226}Th calculated based on CDFT in OCHO and TCHO bases. Obviously, the total flux rises more rapidly for the calculation based on TCHO. This is easy to understand because the current is sensitive to the potential barrier, while a lower barrier is obtained by TCHO. The charge yields in Fig. 6(b) calculated based on both TCHO and OCHO can reproduce the trend of the experimental data, especially the coexistence of symmetric and asymmetric peaks in experimental data. Although the peak values are still away from the data, however, the TCHO calculation presents a trend to improve the description: The asymmetric fission peak value decreases from 15.07% to 13.76% and the dip at $Z \approx 40$, 50

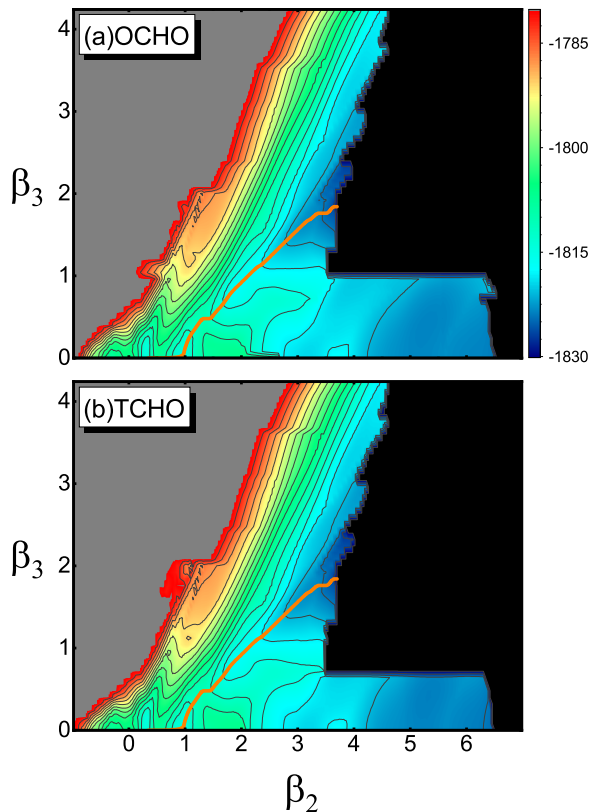


FIG. 7. Same as Fig. 2 but for ^{240}Pu .

increases from 1.66% to 1.96%, which can be attributed to a reduction of the ridge between asymmetric and symmetric fission valleys (cf. Fig. 2).

B. Results for ^{240}Pu

Figure 7 displays the PESs of ^{240}Pu in the β_2 - β_3 plane calculated using the CDFT in OCHO and TCHO bases. Along the static fission path, the heights of the first fission barrier are 6.79 MeV (OCHO) and 6.83 MeV (TCHO), while they are 3.62 MeV (OCHO) and 3.76 MeV (TCHO) for the outer barrier. Note that TCHO predicts higher fission barriers for ^{240}Pu , different from the case in ^{226}Th . For the region with $\beta_3 \approx 0.88$, the calculated two PESs for ^{240}Pu are quite different: Scission happens much earlier in the TCHO calculation than in that of OCHO. To understand the difference, we will analyze the PES in a higher dimension by introducing a constraint on the particle number in the neck q_N . Figure 8 displays the PES in the β_2 - q_N plane with a fixed $\beta_3 = 0.88$ calculated by CDFT-TCHO. The solid curve denotes the fission path without constraint on q_N . For comparison, we also show the corresponding fission path calculated by CDFT-OCHO, denoted by the dashed curve. It is interesting to find that the nucleus goes to different fission valleys in the two calculations due to the subtle difference.

Furthermore, it is interesting to compare the present PES to those calculated from nonrelativistic DFT with the Skyrme SkM* and Gogny D1S functionals for the benchmark nucleus ^{240}Pu [22]. All functionals yield similar binding energies and

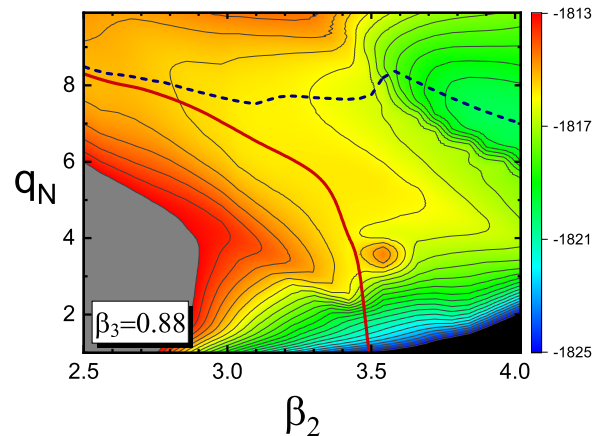


FIG. 8. Potential energy surfaces of ^{240}Pu in the β_2 - q_N plane for a fixed $\beta_3 = 0.88$ calculated by CDFT-TCHO with PC-PK1 functional. The solid curve denotes the fission path without constraint on q_N . For comparison, the corresponding fission path calculated by CDFT-OCHO is also shown as a dashed curve.

deformations for the equilibrium state, indicating that the relativistic correction to the bulk properties of the ground state is small. However, there are significant differences in the scission configurations predicted by CDFT, showing larger elongation for symmetric fission and a more intricate structure for asymmetric fission. These disparities arise from variations in the underlying single-particle levels, particularly the spin-orbital splitting that can be self-consistently handled within the relativistic framework. The distinct scission configurations may have implications for the description of fission observables such as fragment yields, TKEs, excitation energies of fragments, and more.

The fission yield distribution calculated by TDGCM+GOA is shown in Fig. 9 and compared with the experimental data [69], while the initial state is prepared by simulating the initial state as a Gaussian superposition of collective eigenmodes in an extrapolated first potential

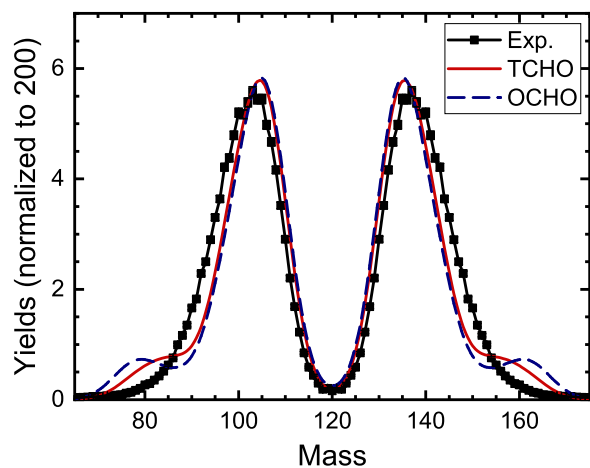


FIG. 9. Mass distributions of the nascent fragments of ^{240}Pu calculated by TDGCM+GOA based on OCHO and TCHO, in comparison with the experimental data [69].

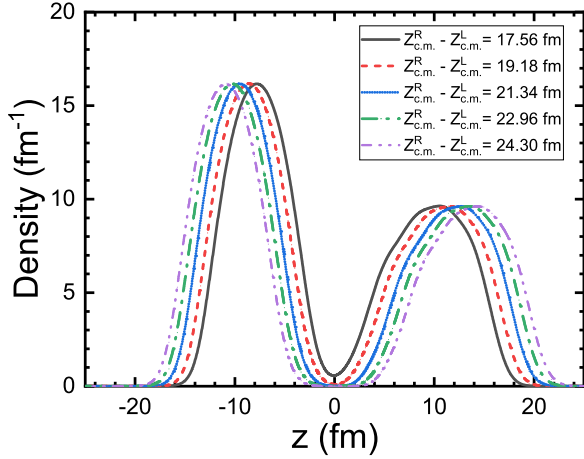


FIG. 10. The density distributions of ^{240}Pu along z axis for the scission point and beyond. The black solid line denotes the density for scission point and the other lines from inside to outside indicate those for the configurations, with the distance between the mass centers of the left and right nascent fragments gradually increasing to 19.18, 21.34, 22.96, 24.30 fm.

well, and the average energy lies 1 MeV higher than the inner fission barrier. The fission yield distribution presents double peaks, and both the peak values and peak positions are in good agreement with the experimental data. In the area with large mass asymmetry, two weak peaks are predicted in the calculation based on OCHO, which may be due to the too soft PES at the region with both large β_2 and β_3 . Obviously, this has been modified in the calculation based on TCHO.

IV. DENSITY CONSTRAINT CALCULATION FOR POSTSCISSION

In a general fission process, starting from the excitation of the mother nucleus, scission usually occurs within 10^{-20} seconds. Then, the fragments are far away from each other, and the fast neutron is emitted after about 10^{-17} seconds. The huge difference between the two timescales allows us to assume that the configurations of the two nascent fragments will not change much in a short time after scission. Therefore, to simulate the splitting process of the nascent fragments beyond scission, we will introduce a density constraint in the new CDFT framework:

$$\langle E_{\text{tot}} \rangle + C_\rho \left(\int \rho(r_\perp, z) - \rho_0(r_\perp, z) dr \right)^2, \quad (34)$$

where C_ρ is the corresponding stiffness constant, and ρ and ρ_0 are the calculated and target densities of the nucleons, respectively. The target density can be chosen as the one of scission configuration, but splitting the two fragments by a certain distance along the z direction with the center of mass fixed at $z = 0$. Figure 10 displays the variation of the density distribution of ^{240}Pu along the z axis from scission point to large separation. Obviously, this method can simulate the fission procedure smoothly after scission and keep the properties of nascent fragments at scission. This is almost impossible in CDFT-OCHO since the two fragments are separated.

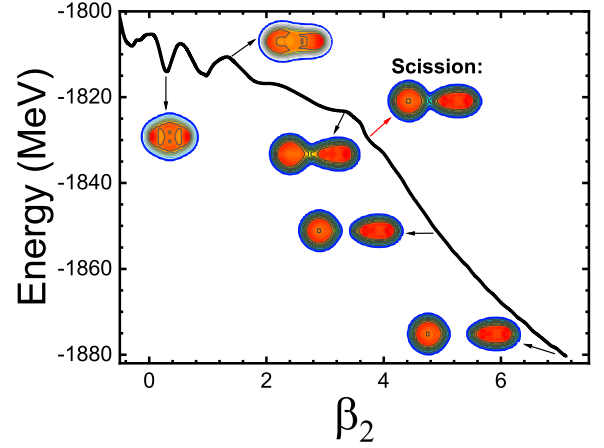


FIG. 11. The potential energy curve of ^{240}Pu along the optimal fission path including both precission and postscission configurations. Contour plots of density distributions for some selected configurations are also shown.

Figure 11 displays the potential energy curve of ^{240}Pu along the optimal fission path including both precission and postscission configurations. Contour plots of density distributions for some selected configurations are also shown. Precission configurations correspond to those denoted by the orange curve in Fig. 7(b), while the postscission configurations are obtained by density constraint calculation. Starting from the ground state with ellipsoidal deformation, the nucleus passes through two fission barriers, drops rapidly to the scission point, and finally separates under Coulomb repulsion. This provides a full space to analyze the generation and evolution of the angular momentum of the fragments during the whole fission procedure, a work that is currently in progress.

V. SUMMARY AND OUTLOOK

We have extended the point-coupling CDFT to be based on the TCHO basis and performed illustrative calculations for the PESs and induced fission dynamics of two typical examples: ^{226}Th and ^{240}Pu . A more reasonable PES is obtained in the new framework compared to that based on OCHO with the same basis space, especially for the outer fission barriers and large elongated configurations, with an optimization of about 0.2–0.3 MeV. When compared to nonrelativistic calculations, CDFT predicts significant differences in the scission configurations for the benchmark nucleus ^{240}Pu : Larger elongation for symmetric fission and a more intricate structure for asymmetric fission. These disparities arise from variations in the underlying single-particle levels, particularly the spin-orbital splitting that can be self-consistently handled within the relativistic framework. Using the PESs, mass tensor, and scission configurations as inputs, we have also simulated the dynamics for the induced fission of ^{226}Th and ^{240}Pu in the framework of TDGCM+GOA. The dynamical simulations based on CDFT-TCHO show an improved description of fission yields. Finally, we also introduced a density constraint into the new framework to simulate the postscission procedure by separating the two frozen fragments from the scission point. This

provides a full space to analyze the generation and evolution of the angular momentum of the fragments during the whole fission procedure, a work that is currently in progress.

The newly developed CDFT-TCHO optimizes the elongated configurations, improves the calculation efficiency, and provides a basis for large-scale multidimensional constraint calculation. Very recently, we performed a fully three-dimensional (3D) calculation to generate the 3D PES for the fission of compound nucleus ^{236}U using CDFT-TCHO with constraints on the axial quadrupole and octupole deformations (β_2, β_3) as well as the nucleon number in the neck, q_N [70]. By considering the additional degree of freedom q_N , the PES broadens up to form a wide “estuary” in the (β_2, q_N) subspace for $q_N < 6$: the energy surface is very shallow across a large range of quadrupole deformations. This leads to a fluctuation for the estimated total kinetic energies by several to ten MeV and for the fragment masses by several to about ten nucleons. Of course, this is just a simple estimation for the fluctuation of the fission observables. More precise analysis should be done by performing 3D TDGCM+GOA calculation based on the 3D PES.

Furthermore, the cluster formation and emission within the relativistic framework is an interesting issue. It has been demonstrated that the relativistic functionals are characterized by deep single-nucleon potentials, which predict the occurrence of much more pronounced cluster structures when compared to non-relativistic functionals that yield similar ground-state properties (binding energy, deformation, radii) [71]. Recently, time-dependent density functional theory based on a relativistic energy density functional was used to analyze the final phase of the process of induced fission of ^{240}Pu , and showed that the timescale of neck formation coincides with the assembly of two α -like clusters, which could also be linked to ternary fission [45]. The newly developed CDFT-TCHO model enables more efficient calculations for a wide array of configurations, making it a valuable tool for studying phenomena such as cluster emission, ternary fission, and other related physical processes. Moreover, the relativistic effects on fission, cluster emission, and ternary fission could be explored by reducing the relativistic framework to a non-relativistic framework [72,73].

ACKNOWLEDGMENTS

This work was partly supported by the National Natural Science Foundation of China (Grants No. 11875225, No. 11790325, No. 11790320, and No. 12375126), the Fundamental Research Funds for the Central Universities, the Fok Ying-Tong Education Foundation, the Continuous-Support Basic Scientific Research Project (BJ010261223282), and National Key R & D Program of China (No. 2022YFA1602000).

APPENDIX: DETERMINATION OF THE PARAMETERS IN TCHO BASIS

In Sec. II B, we introduced the TCHO basis and the expansion of Dirac equation in detail. Here, we will briefly

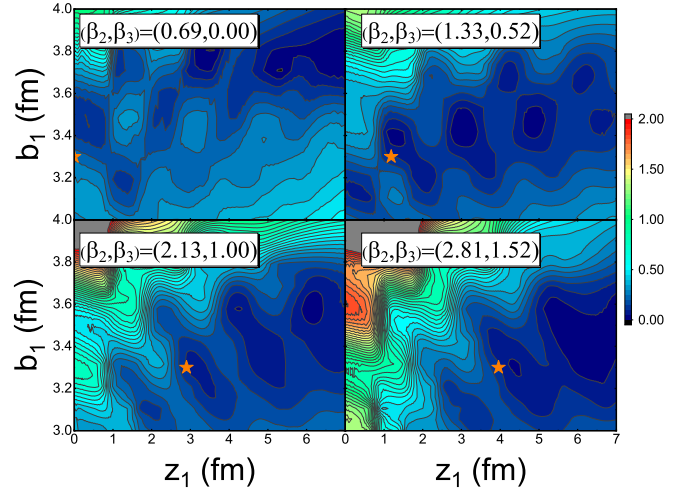


FIG. 12. The total binding energies for some selected configurations of ^{226}Th optimal fission path calculated by CDFT-TCHO using different basis parameters z_1 and b_1 . All energies are normalized with respect to the binding energy of the corresponding global minimum. The energy difference between adjacent contour lines is 0.05 MeV. The stars denote the basis parameters determined by Eqs. (A1) and (A2).

introduce how to determine the two parameters z_1 and b_1 in the TCHO basis. Figure 12 displays the total binding energies for some selected configurations of the ^{226}Th optimal fission path calculated by CDFT-TCHO using different basis parameters z_1 and b_1 . All energies are normalized with respect to the binding energy of the corresponding global minimum. Obviously, we can observe some regions with lowest binding energies in the z_1 - b_1 plane, and these regions move to large z_1 but stay around $b_1 \approx 3.3$ fm as the deformation increases. For the convenience of practical application, we have comprehensively considered the symmetric fission path and the optimal fission path, and summarized the following formulas for the two parameters:

$$z_1 = \begin{cases} 0, & \beta_2 < 1, \\ 3.05\sqrt{1.68\beta_2 - 1.40} - 1.60, & \beta_2 > 1, \end{cases} \quad (\text{A1})$$

$$b_1 = \begin{cases} b_z, & \beta_2 < 0, \\ (b_z - 3.3)\beta_2^2 + (6.6 - 2b_z)\beta_2 + b_z, & 0 < \beta_2 < 1, \\ 3.3, & \beta_2 > 1, \end{cases} \quad (\text{A2})$$

where b_z is the corresponding characteristic length related to the frequency of the spherical harmonic oscillator $\hbar\omega = 41A^{-1/3}$. For configurations with small deformations, TCHO reduces to OCHO ($z_1 = z_2 = 0$). As the nucleus elongates and the two fragments are forming, the basis employed gradually changes from one center to two center, ensuring consistency with the evolving density distribution. The efficiency of these formulas has also been confirmed in the calculations for a number of heavy nuclei.

- [1] N. Schunck and L. M. Robledo, Microscopic theory of nuclear fission: a review, *Rep. Prog. Phys.* **79**, 116301 (2016).
- [2] H. J. Krappe and K. Pomorski, *Theory of Nuclear Fission* (Springer-Verlag, Berlin, 2012).
- [3] N. Bohr and J. A. Wheeler, The mechanism of nuclear fission, *Phys. Rev.* **56**, 426 (1939).
- [4] M. Brack, J. Damgaard, A. S. Jensen, H. C. Pauli, V. M. Strutinsky, and C. Y. Wong, Funny hills: The shell-correction approach to nuclear shell effects and its applications to the fission process, *Rev. Mod. Phys.* **44**, 320 (1972).
- [5] J. R. Nix, Calculation of fission barriers for heavy and super-heavy nuclei, *Annu. Rev. Nucl. Sci.* **22**, 65 (1972).
- [6] P. Moller, D. Madland, A. Sierk, and A. Iwamoto, Nuclear fission modes and fragment mass asymmetries in a five-dimensional deformation space, *Nature (London)* **409**, 785 (2001).
- [7] P. Möller, A. J. Sierk, T. Ichikawa, A. Iwamoto, R. Bengtsson, H. Uhrenholt, and S. Åberg, Heavy-element fission barriers, *Phys. Rev. C* **79**, 064304 (2009).
- [8] T. Ichikawa, A. Iwamoto, P. Möller, and A. J. Sierk, Contrasting fission potential-energy structure of actinides and mercury isotopes, *Phys. Rev. C* **86**, 024610 (2012).
- [9] P. Jachimowicz, M. Kowal, and J. Skalski, Secondary fission barriers in even-even actinide nuclei, *Phys. Rev. C* **85**, 034305 (2012).
- [10] P. Jachimowicz, M. Kowal, and J. Skalski, Eight-dimensional calculations of the third barrier in ^{232}Th , *Phys. Rev. C* **87**, 044308 (2013).
- [11] Z.-M. Wang, W.-J. Zhu, X. Zhu, C.-L. Zhong, and T.-S. Fan, ^{236}U multi-modal fission paths on a five-dimensional deformation surface, *Commun. Theor. Phys.* **71**, 417 (2019).
- [12] X. Zhu, Z.-M. Wang, W.-J. Zhu, C.-L. Zhong, Y.-M. Zhang, L.-Y. Liao, and T.-S. Fan, Macroscopic-microscopic calculations of fission potential surface of uranium isotopes in the three quadratic surfaces parametrization, *Commun. Theor. Phys.* **72**, 105301 (2020).
- [13] C. Schmitt, K. Pomorski, B. Nerlo-Pomorska, and J. Bartel, Performance of the Fourier shape parametrization for the fission process, *Phys. Rev. C* **95**, 034612 (2017).
- [14] L.-L. Liu, X.-Z. Wu, Y.-J. Chen, C.-W. Shen, Z.-X. Li, and Z.-G. Ge, Study of fission dynamics with a three-dimensional Langevin approach, *Phys. Rev. C* **99**, 044614 (2019).
- [15] K.-H. Schmidt and B. Jurado, Review on the progress in nuclear fission—experimental methods and theoretical descriptions, *Rep. Prog. Phys.* **81**, 106301 (2018).
- [16] C. Simenel and A. Umar, Heavy-ion collisions and fission dynamics with the time-dependent Hartree-Fock theory and its extensions, *Prog. Part. Nucl. Phys.* **103**, 19 (2018).
- [17] M. Bender *et al.*, Future of nuclear fission theory, *J. Phys. G* **47**, 113002 (2020).
- [18] M. Verriere and D. Regnier, The time-dependent generator coordinate method in nuclear physics, *Front. Phys.* **8**, 233 (2020).
- [19] N. Schunck and D. Regnier, Theory of nuclear fission, *Prog. Part. Nucl. Phys.* **125**, 103963 (2022).
- [20] J. Berger, M. Girod, and D. Gogny, Microscopic analysis of collective dynamics in low energy fission, *Nucl. Phys. A* **428**, 23 (1984).
- [21] H. Goutte, J. F. Berger, P. Casoli, and D. Gogny, Microscopic approach of fission dynamics applied to fragment kinetic energy and mass distributions in ^{238}U , *Phys. Rev. C* **71**, 024316 (2005).
- [22] D. Regnier, N. Dubray, N. Schunck, and M. Verrière, Fission fragment charge and mass distributions in $^{239}\text{Pu}(n, f)$ in the adiabatic nuclear energy density functional theory, *Phys. Rev. C* **93**, 054611 (2016).
- [23] D. Regnier, M. Verrière, N. Dubray, and N. Schunck, FELIX-1.0: A finite element solver for the time dependent generator coordinate method with the Gaussian overlap approximation, *Comput. Phys. Commun.* **200**, 350 (2016).
- [24] A. Zdeb, A. Dobrowolski, and M. Warda, Fission dynamics of ^{252}Cf , *Phys. Rev. C* **95**, 054608 (2017).
- [25] D. Regnier, N. Dubray, and N. Schunck, From asymmetric to symmetric fission in the fermium isotopes within the time-dependent generator-coordinate-method formalism, *Phys. Rev. C* **99**, 024611 (2019).
- [26] W. Younes and D. Gogny, Fragment yields calculated in a time-dependent microscopic theory of fission, Lawrence Livermore National Laboratory Technical Report No. LLNL-TR-586678, 2012.
- [27] H. Tao, J. Zhao, Z. P. Li, T. Nikšić, and D. Vretenar, Microscopic study of induced fission dynamics of ^{226}Th with covariant energy density functionals, *Phys. Rev. C* **96**, 024319 (2017).
- [28] J. Zhao, T. Nikšić, D. Vretenar, and S.-G. Zhou, Microscopic self-consistent description of induced fission dynamics: Finite-temperature effects, *Phys. Rev. C* **99**, 014618 (2019).
- [29] J. Zhao, J. Xiang, Z.-P. Li, T. Nikšić, D. Vretenar, and S.-G. Zhou, Time-dependent generator-coordinate-method study of mass-asymmetric fission of actinides, *Phys. Rev. C* **99**, 054613 (2019).
- [30] J. Zhao, T. Nikšić, and D. Vretenar, Microscopic self-consistent description of induced fission: Dynamical pairing degree of freedom, *Phys. Rev. C* **104**, 044612 (2021).
- [31] J. Zhao, T. Nikšić, and D. Vretenar, Time-dependent generator coordinate method study of fission. II. Total kinetic energy distribution, *Phys. Rev. C* **106**, 054609 (2022).
- [32] Y.-J. Chen, Y. Su, G. Dong, L.-L. Liu, Z. Ge, and X. Wang, Energy density functional analysis of the fission properties of ^{240}Pu : The effect of pairing correlations, *Chin. Phys. C* **46**, 024103 (2022).
- [33] Y.-J. Chen, Y. Su, L.-L. Liu, G. Dong, Z. Ge, N. Shu, and X. Wang, Microscopic study of neutron-induced fission process of ^{239}Pu via zero- and finite-temperature density functional theory, *Chin. Phys. C* **47**, 054103 (2023).
- [34] X. B. Wang, Y. Chen, G. X. Dong, Y. Su, Z. Li, X. Z. Wu, and Z. X. Li, Role of pairing correlations in the fission process, *Phys. Rev. C* **108**, 034306 (2023).
- [35] N. Schunck, M. Verriere, G. Potel Aguilar, R. C. Malone, J. A. Silano, A. P. D. Ramirez, and A. P. Tonchev, Microscopic calculation of fission product yields for odd-mass nuclei, *Phys. Rev. C* **107**, 044312 (2023).
- [36] A. Bulgac, P. Magierski, K. J. Roche, and I. Stetcu, Induced fission of ^{240}Pu within a real-time microscopic framework, *Phys. Rev. Lett.* **116**, 122504 (2016).
- [37] M. V. Stoitsov, N. Schunck, M. Kortelainen, N. Michel, H. Nam, E. Olsen, J. Sarich, and S. Wild, Axially deformed solution of the Skyrme-Hartree-Fock-Bogoliubov equations using the transformed harmonic oscillator basis (II) HFBTHO v2.00d: A new version of the program, *Comput. Phys. Commun.* **184**, 1592 (2013).
- [38] N. Schunck, J. Dobaczewski, J. McDonnell, W. Satuła, J. Sheikh, A. Staszczak, M. Stoitsov, and P. Toivanen, Solution of

- the Skyrme-Hartree-Fock-Bogolyubov equations in the Cartesian deformed harmonic-oscillator basis.: (VII) HFODD (v2.49t): A new version of the program, *Comput. Phys. Commun.* **183**, 166 (2012).
- [39] N. Schunck, J. Dobaczewski, W. Satula, P. Baczyk, J. Dudek, Y. Gao, M. Konieczka, K. Sato, Y. Shi, X. B. Wang, and T. R. Werner, Solution of the Skyrme-Hartree-Fock-Bogolyubov equations in the Cartesian deformed harmonic-oscillator basis. (VIII) HFODD (v2.73y): A new version of the program, *Comput. Phys. Commun.* **216**, 145 (2017).
- [40] P.-G. Reinhard, B. Schuetrumpf, and J. A. Maruhn, The axial Hartree-Fock plus BCS code SkyAx, *Comput. Phys. Commun.* **258**, 107603 (2021).
- [41] M. Warda, J. L. Egido, L. M. Robledo, and K. Pomorski, Self-consistent calculations of fission barriers in the Fm region, *Phys. Rev. C* **66**, 014310 (2002).
- [42] W. Younes and D. Gogny, Microscopic calculation of ^{240}Pu scission with a finite-range effective force, *Phys. Rev. C* **80**, 054313 (2009).
- [43] B.-N. Lu, J. Zhao, E.-G. Zhao, and S.-G. Zhou, Multidimensionally constrained relativistic mean-field models and potential-energy surfaces of actinide nuclei, *Phys. Rev. C* **89**, 014323 (2014).
- [44] Z. X. Ren, P. W. Zhao, and J. Meng, Time-dependent covariant density functional theory in three-dimensional lattice space: Benchmark calculation for the $^{16}\text{O}+^{16}\text{O}$ reaction, *Phys. Rev. C* **102**, 044603 (2020).
- [45] Z. X. Ren, D. Vretenar, T. Nikšić, P. W. Zhao, J. Zhao, and J. Meng, Dynamical synthesis of ^4He in the scission phase of nuclear fission, *Phys. Rev. Lett.* **128**, 172501 (2022).
- [46] J. Zhao, B.-N. Lu, T. Nikšić, and D. Vretenar, Multidimensionally constrained relativistic Hartree-Bogolyubov study of spontaneous nuclear fission, *Phys. Rev. C* **92**, 064315 (2015).
- [47] J. Zhao, B.-N. Lu, T. Nikšić, D. Vretenar, and S.-G. Zhou, Multidimensionally-constrained relativistic mean-field study of spontaneous fission: Coupling between shape and pairing degrees of freedom, *Phys. Rev. C* **93**, 044315 (2016).
- [48] Z. Li, S. Chen, Y. Chen, and Z. Li, Microscopic study on asymmetric fission dynamics of ^{180}Hg within covariant density functional theory, *Phys. Rev. C* **106**, 024307 (2022).
- [49] J.-F. Berger, Self-consistent microscopic approach for low-energy large amplitude collective processes in nuclei: application to heavy-ion scattering and fission, Ph.D. thesis, Université Paris-Sud, 1985.
- [50] L.-S. Geng, J. Meng, and H. Toki, Reflection asymmetric relativistic mean field approach and its application to the octupole deformed nucleus ^{226}Ra , *Chin. Phys. Lett.* **24**, 1865 (2007).
- [51] L.-S. Geng, The study of ground state properties and octupole deformation in atomic nuclei using the relativistic mean field theory, Ph.D. thesis, Peking University, 2007.
- [52] X.-L. Ren, K.-W. Li, L.-S. Geng, B. Long, P. Ring, and J. Meng, Leading order relativistic chiral nucleon-nucleon interaction, *Chin. Phys. C* **42**, 014103 (2018).
- [53] J. Meng, *Relativistic Density Functional for Nuclear Structure* (World Scientific, Singapore, 2016).
- [54] J. Meng and P. Zhao, Relativistic density functional theory in nuclear physics, *AAPPS Bulletin* **31**, 2 (2021).
- [55] Y. Wang, F. Xu, T. Huang, and P. Zhao, Relativistic density functional theory in nuclear physics, *Chin. Sci. Bull.* **68**, 1074 (2023).
- [56] P. W. Zhao, Z. P. Li, J. M. Yao, and J. Meng, New parametrization for the nuclear covariant energy density functional with a point-coupling interaction, *Phys. Rev. C* **82**, 054319 (2010).
- [57] C. G. Broyden, A class of methods for solving nonlinear simultaneous equations, *Math. Comput.* **19**, 577 (1965).
- [58] A. Baran, A. Bulgac, M. M. Forbes, G. Hagen, W. Nazarewicz, N. Schunck, and M. V. Stoitsov, Broyden's method in nuclear structure calculations, *Phys. Rev. C* **78**, 014318 (2008).
- [59] T. Bürvenich, D. G. Madland, J. A. Maruhn, and P.-G. Reinhard, Nuclear ground state observables and qcd scaling in a refined relativistic point coupling model, *Phys. Rev. C* **65**, 044308 (2002).
- [60] K. Hagino and T. Ichikawa, New and efficient method for solving the eigenvalue problem for the two-center shell model with finite-depth potentials, *Phys. Rev. C* **95**, 054620 (2017).
- [61] M. Girod and B. Grammaticos, The zero-point energy correction and its effect on nuclear dynamics, *Nucl. Phys. A* **330**, 40 (1979).
- [62] D. R. Inglis, Nuclear moments of inertia due to nucleon motion in a rotating well, *Phys. Rev.* **103**, 1786 (1956).
- [63] S. Beliaev, Concerning the calculation of the nuclear moment of inertia, *Nucl. Phys.* **24**, 322 (1961).
- [64] Z. P. Li and D. Vretenar, Model for collective motion, in *Handbook of Nuclear Physics*, edited by I. Tanihata, H. Toki, and T. Kajino (Springer Nature, Singapore, 2020), pp. 1–33.
- [65] D. Regnier, N. Dubray, M. Verrière, and N. Schunck, Felix-2.0: New version of the finite element solver for the time dependent generator coordinate method with the gaussian overlap approximation, *Comput. Phys. Commun.* **225**, 180 (2018).
- [66] M. Bender, K. Rutz, P. G. Reinhard, and J. A. Maruhn, Pairing gaps from nuclear mean-field models, *Eur. Phys. J. A* **8**, 59 (2000).
- [67] N. Dubray, H. Goutte, and J.-P. Delaroche, Structure properties of ^{226}Th and $^{256,258,260}\text{Fm}$ fission fragments: Mean-field analysis with the Gogny force, *Phys. Rev. C* **77**, 014310 (2008).
- [68] K.-H. Schmidt, S. Steinhäuser *et al.*, Relativistic radioactive beams: A new access to nuclear-fission studies, *Nucl. Phys. A* **665**, 221 (2000).
- [69] C. Tsuchiya, Y. Nakagome *et al.*, Simultaneous measurement of prompt neutrons and fission fragments for $^{239}\text{Pu}(n_{th}, f)$, *J. Nucl. Sci. Technol.* **37**, 941 (2000).
- [70] M.-H. Zhou, Z.-Y. Li, S.-Y. Chen, Y.-J. Chen, and Z.-P. Li, Three-dimensional potential energy surface for fission of ^{236}U within covariant density functional theory, *Chin. Phys. C* **47**, 064106 (2023).
- [71] J. P. Ebran, E. Khan, T. Nikšić, and D. Vretenar, How atomic nuclei cluster, *Nature (London)* **487**, 341 (2012).
- [72] Y. Guo and H. Liang, Non-relativistic expansion of single-nucleon Dirac equation: Comparison between Foldy-Wouthuysen transformation and similarity renormalization group, *Chin. Phys. C* **43**, 114105 (2019).
- [73] Z. X. Ren and P. W. Zhao, Toward a bridge between relativistic and nonrelativistic density functional theories for nuclei, *Phys. Rev. C* **102**, 021301(R) (2020).